High sensitive and stable self-powered solar-blind photodetector based on solution-processed all inorganic CuMO$_2$/Ga$_2$O$_3$ pn heterojunction

Chao Wu [a,1], Linlin Qiu [b,1], Shan Li [d], Daoyou Guo [a,c,*], Peigang Li [d], Shunli Wang [a], Pingfan Du [b], Zhengwei Chen [c,e], Aiping Liu [a,**], Xianghu Wang [f], Huaping Wu [g], Fengmin Wu [a,***], Weihua Tang [d,e]

[a] Center for Optoelectronics Materials and Devices & Key Laboratory of Optical Field Manipulation of Zhejiang Province Department of Physics Zhejiang Sci-Tech University, Hangzhou, 310018, China
[b] College of Textile Science and Engineering, Zhejiang Sci-Tech University, Hangzhou, 310018, PR China
[c] State Key Lab of Silicon Materials, Zhejiang University, Hangzhou, 310027, China
[d] State Key Laboratory of Information Photonics and Optical Communications & Laboratory of Information Functional Materials and Devices School of Science Beijing University of Posts and Telecommunications, Beijing 100876, China
[e] Beijing Gallium Family Technology Ltd., Beijing, 100876, China
[f] College of Materials, Shanghai Dianji University, Shanghai, 201306, PR China
[g] Key Laboratory of Special Purpose Equipment and Advanced Processing Technology, Ministry of Education and Zhejiang Province, College of Mechanical Engineering, Zhejiang University of Technology, Hangzhou, 310023, China

ARTICLE INFO

ABSTRACT

Solar-blind photodetection systems, which can convert solar-blind deep ultraviolet light into an electrical signal, have been designed for practical use owing to their high sensitivity and accuracy. As one of the most suitable semiconductors for solar-blind photodetection, β-Ga$_2$O$_3$ can construct a *pn* type photodetector with another semiconductor material to meet the demands of energy savings, miniaturization and high efficiency. As a kind of natural *p*-type material, delafossite semiconductor materials CuMO$_2$ (M = Al^{3+}, Ga^{3+}, In^{3+}, Cr^{3+}) have attracted much attention recently. The band alignment of CuMO$_2$ is staggered with that of n-type β-Ga$_2$O$_3$; hence, the photogenerated electrons and holes tend to transfer through the interface in the opposite directions, resulting in spatial separation of charge carriers. Meanwhile, the fast hole diffusion coefficient (10^{-2}–10^1 cm^2 V^{-1} s^{-1}) of CuMO$_2$ guarantees the transport of holes, which is difficult in β-Ga$_2$O$_3$ owing to its intrinsic electronic structure. More importantly, compared with the widely used p-type materials, CuMO$_2$ materials are almost insensitive to UVA light owing to the forbidden intrinsic direct transitions between the conduction and valence bands. Hence, the CuMO$_2$/β-Ga$_2$O$_3$ pn junction photodetector exhibits high sensitivity, and the working spectral region is not extended to the UVA region. In this study, n-β-Ga$_2$O$_3$/p-CuMO$_2$ (M: Ga^{3+}, Cr^{3+}) pn junction photodetectors were prepared by a simple solution process method. Due to the high crystallinity of the as-grown CuGaO$_2$ and CuCrO$_2$, the CuGaO$_2$/β-Ga$_2$O$_3$ and CuCrO$_2$/β-Ga$_2$O$_3$ pn junction photodetectors demonstrate an ultralow off state current of 51/61 fA, a superhigh on-to-off state current ratio of 2.3 × 10^4/3.5 × 10^4 and a high rejection ratio (R$_{254}$/R$_{365}$) of 2 × 10^4/2.8 × 10^4 under a bias of 0 V. The CuMO$_2$/β-Ga$_2$O$_3$ pn junction photodetector satisfies the requirements of high sensitivity, stable and energy saving and has wide practical application prospect in solar-blind detection systems.

© 2020 Elsevier Ltd. All rights reserved.

---

* Corresponding author. Center for Optoelectronics Materials and Devices & Key Laboratory of Optical Field Manipulation of Zhejiang Province Department of Physics Zhejiang Sci-Tech University, Hangzhou, 310018, China.
** Corresponding author.
*** Corresponding author.
    E-mail addresses: dyguo@zstu.edu.cn (D. Guo), liuaiping1979@gmail.com (A. Liu), wfm@zstu.edu.cn (F. Wu).
[1] These authors contributed equally.

1. Introduction

Solar-blind detection systems have been designed for practical use in modern optical communication, flame detection, deep ultraviolet imaging, missile guidance and environmental monitoring owing to their high sensitivity and accuracy [1–3]. As important and fundamental building blocks of solar-blind detection systems, solar-blind photodetectors have gained extensive attention. As the most widely used photodetector, Si-based solar-blind photodetectors require the use of expensive filters to block high wavelength photons due to the narrow (1.12 eV) bandgap of Si. In recent decades, numerous ultrawide bandgap semiconductors, such as diamond, AlN, $Al_xGa_{1-x}N$ and $Mg_xZn_{1-x}O$, have met the criteria of a solar-blind photodetector with a cutoff below 280 nm [4-8]. However, the problems of epitaxial growth and bandgap engineering still limit their practical application. Ga_2O_3, especially the most stable β-Ga_2O_3 phase, is a natural solar-blind material due to its ultrawide bandgap (~4.8 eV) [9–18]. Moreover, mature epitaxial technology and doping engineering guarantee its application in the solar-blind detection field [19–23].

To meet the demands for photodetectors of more energy savings, miniaturization and high efficiency, many researchers are seeking to build a self-powered system. An energy savings photodetector can be driven by a built-in electric field, which is mainly provided by a pn homojunction, a pn heterojunction or a Schottky junction. As the most used structure, the pn junction can be fabricated on the substrate by deposited p-type semiconductor and n-type semiconductor, respectively, and the space charge area is formed at their interface by carrier diffusion effect [24–38]. However, it is still challenging to synthesize *p*-type Ga_2O_3, and hence, finding a suitable *p*-type material is crucial to designing a Ga_2O_3-based self-powered photodetector.

Delafossite semiconductor materials $CuMO_2$ (M = Al^{3+}, Ga^{3+}, In^{3+}, Cr^{3+}) have attracted much attention owing to their wide bandgap and fast hole diffusion coefficient [39–41]. Recently, they have been widely used in variety of optoelectronic fields, such as transparent conducting oxides, solar cells, and catalysts [42–51]. However, there are few reports in the photodetector field[44][52][54][53]. $CuMO_2$ materials are suitable for constructing a pn junction with β-Ga_2O_3 for the following reasons: 1) The band alignment of $CuMO_2$ is staggered with that of n-type β-Ga_2O_3, hence the photogenerated electrons and holes tend to transfer through the interface in the opposite directions, resulting in spatial separation of charge carriers. 2) β-Ga_2O_3 has low hole mobility owing to its intrinsic electronic structure, while the fast hole diffusion coefficient of $CuMO_2$ can guarantee the transport of holes. 3) Highly

crystalline $CuMO_2$ can be obtained through a convenient and cost-efficient solution growth process. More importantly, in comparison with the widely used p-type materials, $CuMO_2$ materials are almost insensitive to UVA light owing to the forbidden intrinsic direct transitions between the conduction and valence bands. Hence, the $CuMO_2/\beta$-Ga_2O_3 pn junction photodetector exhibits high sensitivity, and the working spectral region is not extended to the UVA region.

In this paper, we prepared energy saving solar blind photodetectors based on a $CuMO_2/\beta$-Ga_2O_3 (M = Ga^{3+}, Cr^{3+}) pn junction through a simple spin-coating method strategy. Highly crystalline $CuMO_2$ are synthesized successfully by a simple and low-cost hydrothermal method and spin-coated on a β-Ga_2O_3 epitaxial film. The built-in electric field at the $CuMO_2/\beta$-Ga_2O_3 pn junction spontaneously separates photogenerated electron-hole pairs, which makes the photodetectors exhibit self-powered properties under zero bias. Under zero bias, the $CuGaO_2/\beta$-Ga_2O_3 and $CuCrO_2/\beta$-Ga_2O_3 pn photodetectors show a photoresponse time of 0.14 s/0.06 s, a high on-to-off state current ratio (I_{on}/I_{off}) of 2.3 × 10^4/3.5 × 10^4 and a high rejection ratio (R_{254}/R_{365}) of 2.0 × 10^4/2.8 × 10^4. In addition, the achieved photodetectors retain sensitivity to the solar-blind light and an almost unchanged photocurrent over a duration of one month under normal atmospheric storage. These simple, low-cost, high-performance and stable pn heterojunction self-powered photodetectors have great potential applications in the solar-blind light detection system field.

2. Results and discussion

Fig. 1 illustrates the fabrication process of the $CuMO_2/\beta$-Ga_2O_3 (M = Ga^{3+}, Cr^{3+}) pn photodetector. In brief, first, a Ga_2O_3 film is deposited on a (0001) plane sapphire substrate by the metal-organic chemical vapor deposition (MOCVD) method. Then, hydrothermally synthesized $CuMO_2$ is dispersed in isopropanol solution and spin coated on the Ga_2O_3 film. Finally, the electrodes of the hybrid structure are deposited to fabricate a pn junction photodetector (more details can be found in the Experimental Section). Fig. 2b shows the crystal structure of the prepared $CuMO_2$ samples shown in Fig. 2a. X-ray diffraction (XRD) and X-ray photoelectron spectroscopy (XPS) measurements were performed to characterize the crystalline structure and composition of $CuMO_2$. As shown in Fig. 2c, the purity of the samples were confirmed by indexing all diffraction peaks with rhombohedral structure $CuGaO_2$ (JCPDS#41−0255) and $CuCrO_2$ (JCPDS#39−0247). To further confirm the element valence in the $CuMO_2$, X-ray photoelectron spectroscopy was measured. For $CuGaO_2$, peaks locate at 932.3 and
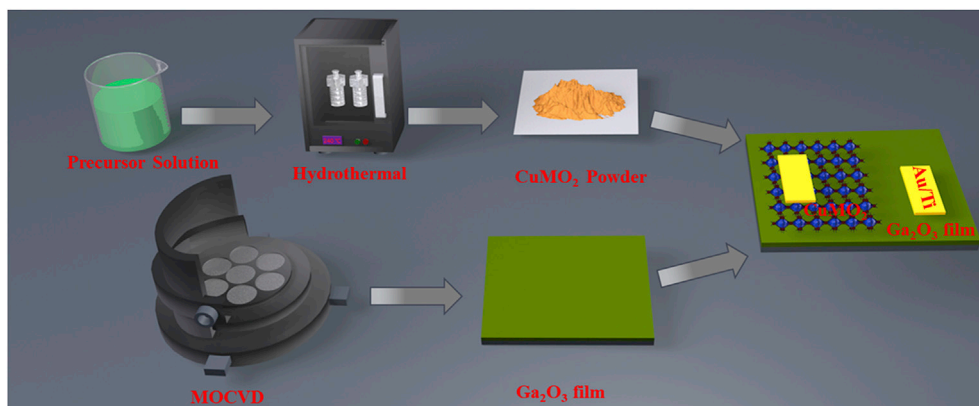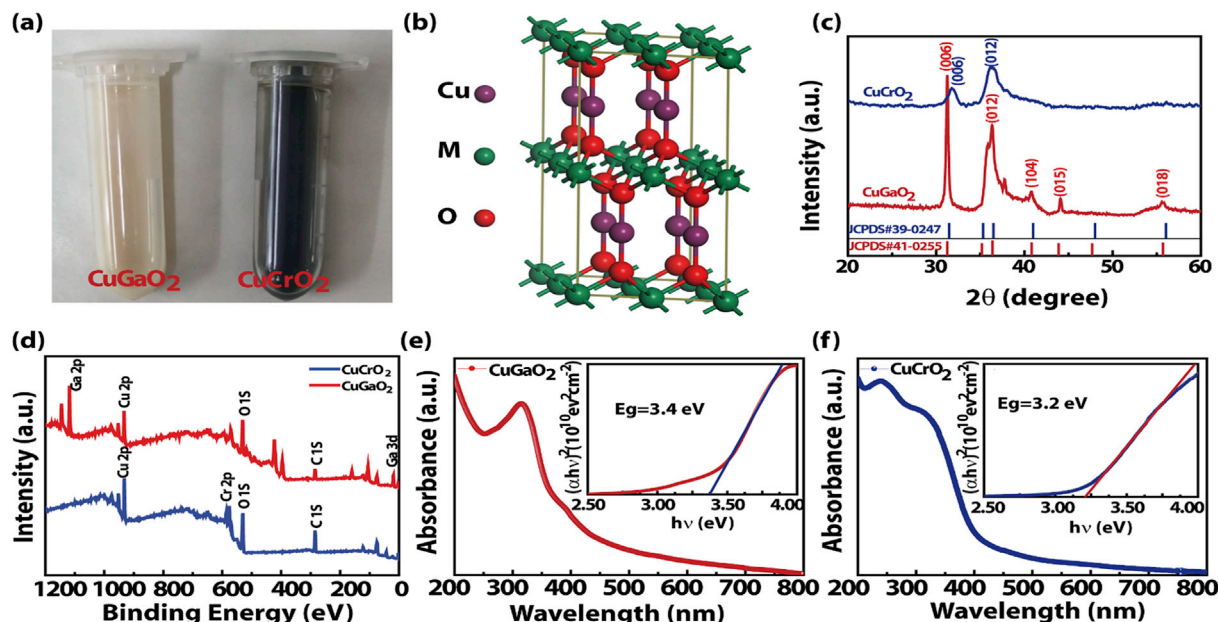

Fig. 1. Schematic illustration of formation of $CuMO_2/\beta$-Ga_2O_3 pn photodetector.

Fig. 2. (a) Optical image of CuGaO$_2$ and CuCrO$_2$ isopropanol solution; (b) Crystal structure of CuMO$_2$; (c) XRD patterns (upper) of the as-grown CuGaO$_2$ and CuCrO$_2$ nanoplates and the standard XRD patterns (bottom) for orthorhombic CuMO$_2$; (d) XPS spectrums of as-grown CuGaO$_2$ and CuCrO$_2$; (e) and (f) the UV−vis spectra of CuGaO$_2$ and CuCrO$_2$ (the inset is the optical band gap).

1118.1 eV are corresponding to Cu$^+$ and Ga^{3+}, respectively. The O 1s peak located at 530.4 eV can be attributed to the lattice oxygen O^{2-} in the crystal lattice. While the oxygen vacancies related peak at about 531.8 eV does not appear, indicating the good quality of the as-grown sample. Similarly, for CuCrO$_2$, a Cr 2p$_{3/2}$ peak was identified at 575.1 eV, corresponding to Cr^{3+} (Fig. 2d) [43,52,55]. The UV−Vis absorption spectra of the CuMO$_2$ are shown in Fig. 2e and f. The corresponding optical bandgaps are about 3.4 eV and 3.2 eV, respectively.

Scanning electron microscopy (SEM), energy dispersive X-ray spectroscopy (EDS) and high-resolution transmission electron microscopy (HRTEM) were applied to further characterize the morphology and structure of the as-grown CuGaO$_2$ and CuCrO$_2$. The CuGaO$_2$ were composed of numerous micrometre-sized 2D micro-plates (Fig. 3a), which is owing to the oriented attachment (OA) growth mechanism [46,56]. During CuGaO$_2$ micro-plates growth, CuGaO$_2$ are crystallized gradually in the precursor solution firstly and then the primary CuGaO$_2$ micro-plates are
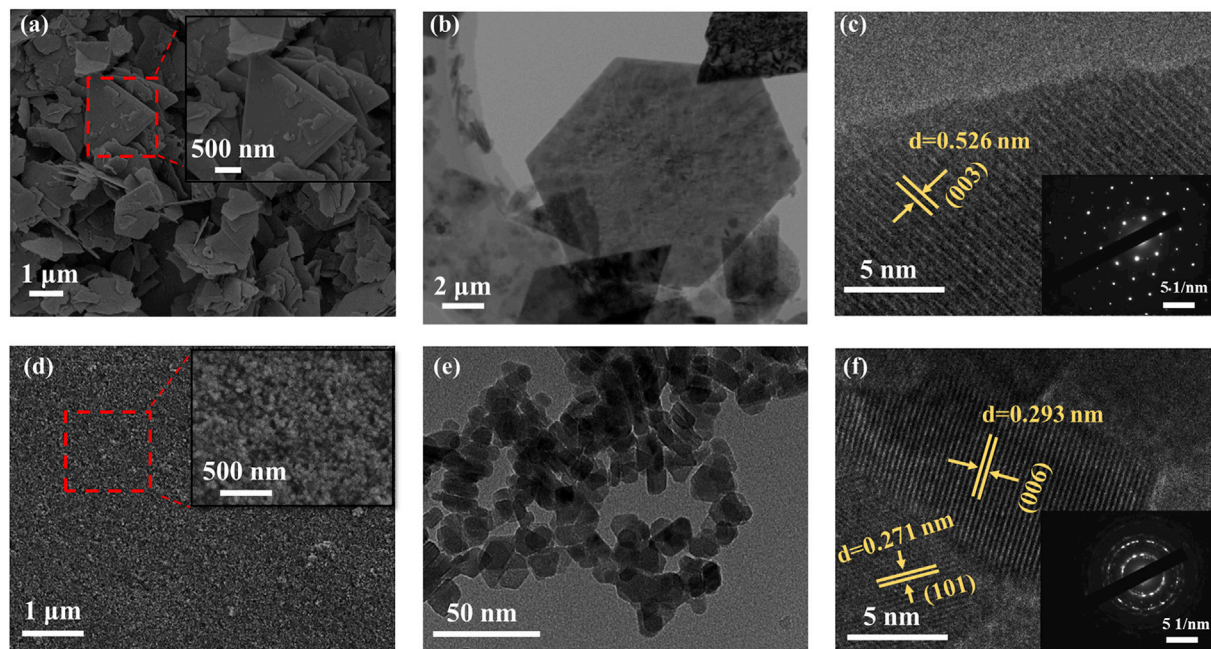
Fig. 3. (a) Typical SEM image of multiple CuGaO$_2$ micro-plates; (b) TEM image of an individual CuGaO$_2$ micro-plate; (c) the corresponding SAED pattern and HRTEM image taken from the CuGaO$_2$ micro-plate. (d) Typical SEM image of multiple CuCrO$_2$ nanoplates; (e) Typical TEM image of an individual CuCrO$_2$ nanoplates; (f) the corresponding SAED pattern and HRTEM image taken from the CuCrO$_2$ nanoplates.

integrated by eliminating the common boundary to form a large particle. As depicted in Fig. 3b, a single $CuGaO_2$ micro-plate exhibits a hexagonal shape with an average diameter of approximately 10 μm. The selected area electron diffraction (SAED) pattern of $CuGaO_2$ further confirms the $CuGaO_2$ micro-plate is single crystallized (Fig. 3c). As shown in the high-resolution FETEM image, the lattice spacing of $CuGaO_2$ is approximately 5.26 Å, which can be indexed to the (003) plane of $CuGaO_2$. Fig. 3d−f shows SEM and TEM images of the obtained $CuCrO_2$ sample. The $CuCrO_2$ consists of ultrasmall nanoplates, which the diameters are approximately 15−25 nm. The 2.71 Å and 2.93 Å interplanar spacings of the $CuCrO_2$ nanoplates are calculated from the high-resolution TEM image, corresponding to the (101) and (006) planes of delafossite $CuCrO_2$, respectively. SFigure 2 shows the elemental maps of individual $CuGaO_2$ micro-plate and $CuCrO_2$ nanoplates. It is evident that Cu, Ga, Cr and O are homogeneously distributed in the micr- or nanoplates.

The characterization of β-Ga_2O_3 layer is shown in SFigure 3. The $(\bar{2}01)$ orientation of the β-Ga_2O_3 film is confirmed by the XRD result, in which only the $(\bar{2}01)$ $(\bar{4}02)$ and $(\bar{6}03)$planes of β-Ga_2O_3 can be observed. The β-Ga_2O_3 epitaxial film shows an obvious absorption edge at approximately 260 nm, corresponding to a bandgap of 4.85 eV (SFigure 3b). The $CuMO_2$/β-Ga_2O_3 pn junction exhibits two absorption edges, which are attributed to the $CuMO_2$ and β-Ga_2O_3 epitaxial films. To further study the chemical states of the β-Ga_2O_3 epitaxial film, the XPS test was performed. As presented in SFigure 3c, characteristic peaks of Ga 3d, C 1s, O 1s and Ga 2p at 20.1, 285.6, 531.08, and 1118.1 eV can be observed. The XPS spectrum of the O 1s core level can be resolved into two separate components. The O_I at 531.4 eV is related to the O^{2-} ions in the lattice, while the O_{II} at 533.5 eV is related to the oxygen vacancies (Vo). The high peak ratio of $O_I/(O_I + O_{II})$ (~88%) guarantees an ultralow dark current of β-Ga_2O_3. Meanwhile, as shown in the AFM image, the β-Ga_2O_3 epitaxial film exhibits a small root-mean-square surface roughness of only 2.17 nm.

After depositing Ti/Au electrodes, $CuMO_2$/β-Ga_2O_3 pn photodetectors were successfully prepared, and their photoelectric performances were investigated. The $CuGaO_2$/β-Ga_2O_3 pn photodetector exhibits a superlow off state current of 100 pA at −5 V and 51 fA at 0 V (Fig. 4a). Owing to the lack of sufficient charger carriers in the Ga_2O_3 epitaxial film with GΩ intrinsic resistance, the rectifying effect under dark conditions is not obvious. Under illumination at a 1000 μW/cm^2 light intensity density 254 nm light, the current increases to 0.54 nA at 0 V, 24.9 nA at −5 V and 2.3 nA at 5 V, exhibiting rectification and self-powered characteristics. For the $CuCrO_2$/β-Ga_2O_3 pn photodetector, the current is 18 pA at −5 V,

61 fA at 0 V and increases to 0.70 nA at 0 V, 27.2 nA at −5 V and 0.8 nA at 5 V under 1000 μW/cm^2 254 nm light irradiation (Fig. 4b). To further investigate the origin of the self-powered and rectifying property of the pn photodetectors, we fabricated and measured the β-Ga_2O_3, $CuGaO_2$ and $CuCrO_2$ based metal-semiconductor-metal photodetectors. As shown in SFigure 4, the linear characteristics of the I−V curves confirm the ohmic contact between β-Ga_2O_3, $CuGaO_2$, $CuCrO_2$ and the Ti/Au electrodes. The ohmic contact property of the single devices verifies that the self-powered manner of $CuMO_2$/β-Ga_2O_3 pn photodetectors originates from the formation of a built-in electric field at pn junction interface.

To systematically assess the performance of $CuMO_2$/β-Ga_2O_3 pn junction photodetectors, their representative I−V and I-T characteristics for different power intensities and applied voltages were researched and presented in Fig. 5 and Fig. 6, respectively. The I−V curves of the $CuGaO_2$/β-Ga_2O_3 pn junction photodetector deviate from the coordinate origin and exhibit a negative photocurrent (Fig. 5a). The photocurrent increases linearly to 0.7 nA as the light intensity density increase to 1000 μW/cm^2, which demonstrates a distinctive augmentation based on the fundamental rule of more absorbed photons producing more free charge carriers (Fig. 5b). Moreover, the high repeatability of the I-T curves demonstrates the sensitive and repeatable response to the light signal of the $CuGaO_2$/β-Ga_2O_3 pn junction photodetector. The on-to-off state current ratio (I_{on}/I_{off}) is related to the signal-to-noise ratio of the photodetector. The I_{on}/I_{off} of the $CuGaO_2$/β-Ga_2O_3 pn junction photodetector at 0 V achieves a superhigh value of 2.3×10^4. The responsivity (R) is usually regarded as an important parameter to evaluate sensitivity of photodetector which can be calculated by the formula $R = (I_{photo} - I_{dark})/(PS)$, where I, P and S represent the current, light intensity density and effective area, respectively. The width of effective area is about 0.3 cm, and the distance between two electrodes is about 0.1 cm, thus the S of the effective irradiation area in our work is counted as 0.03 mm^2 (SFigure 5). As shown in Fig. 5c, the responsivity of the photodetector achieves the maximum value of ~0.025 mA/W at 0 V with light power intensity of 50 μW/cm^2. The ability to detect weak light is another important index for a detector, which is usually measured by the detectivity (D). As shown in Fig. 5d, the maximum D value of 0.9×10^{11} Jones is obtained at 0 V with light power intensity of 50 μW/cm^2. Both of R and D display the gradually declining trend as the power intensity strengthening. The $CuGaO_2$/β-Ga_2O_3 pn junction photodetectors also expresses an excellent device performance under reverse-biased voltages. As shown in Fig. 5e, with the applied voltages increase from −0.5 to −5 V, the photocurrents keep increasing and the I-T curves maintain a highly stable and repeatable shapes. For
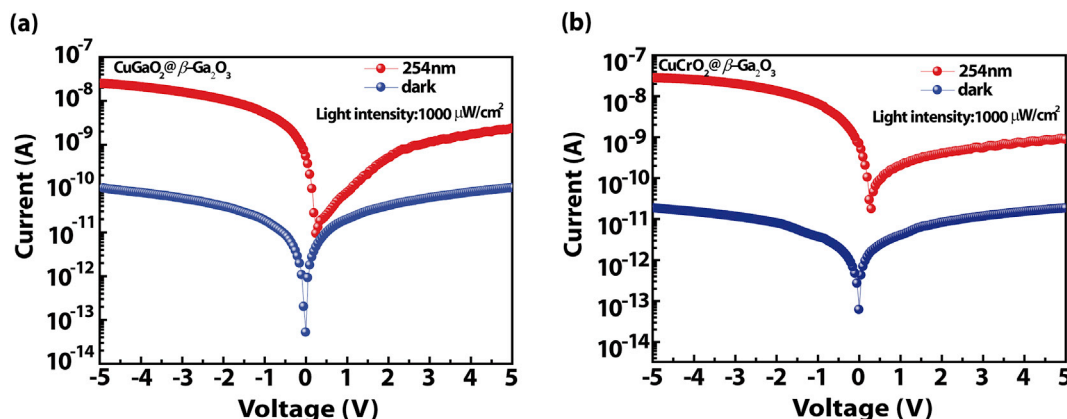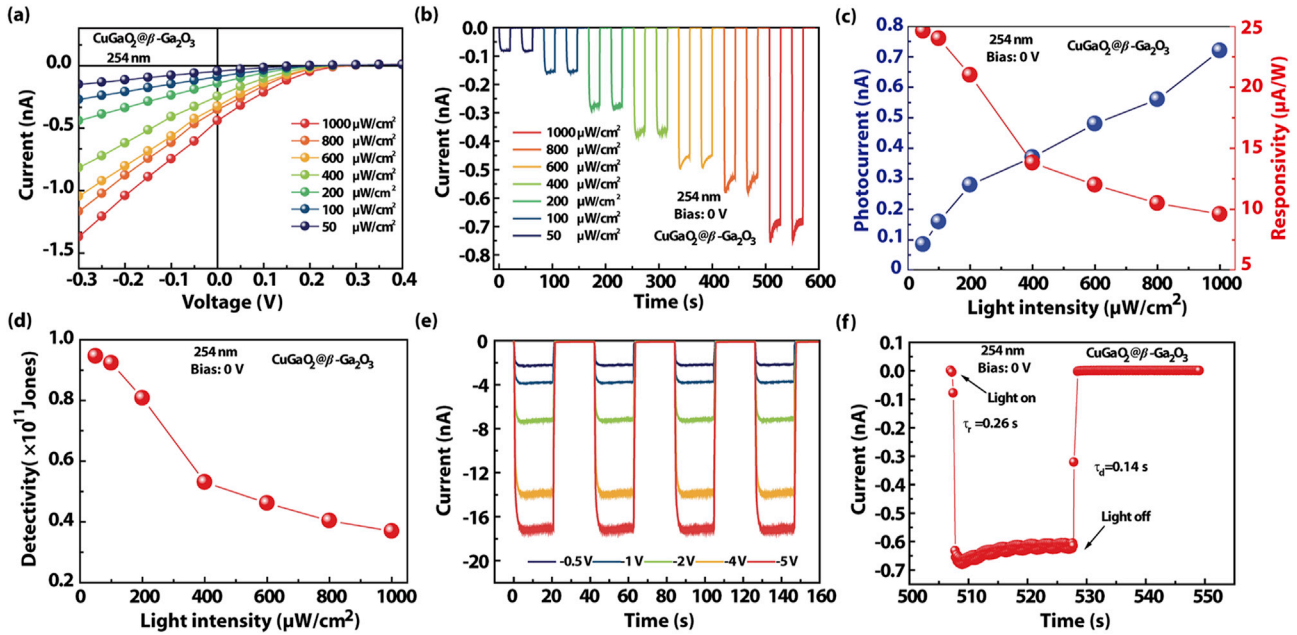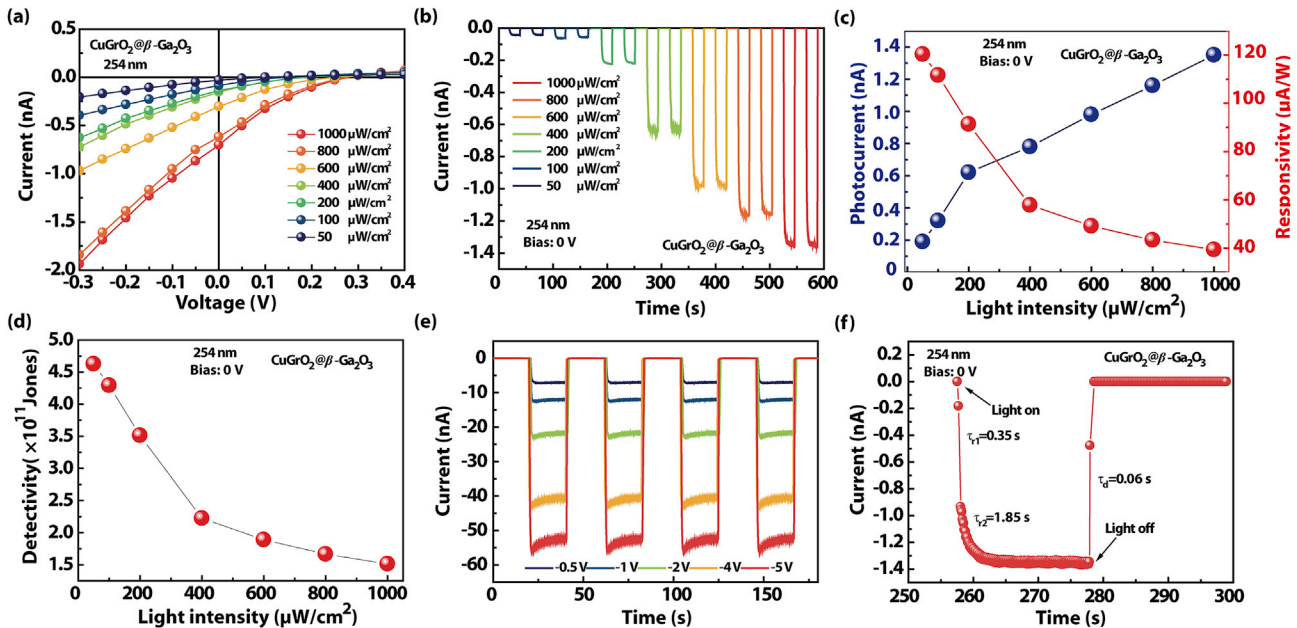

Fig. 4. I−V characteristics of the (a) $CuGaO_2$/β-Ga_2O_3 and (b) $CuCrO_2$/β-Ga_2O_3 pn photodetector under dark and illumination with light-254 nm.

Fig. 5. (a) $I-V$ characteristics of the CuGaO$_2$/β-Ga$_2$O$_3$ pn photodetector under 254 nm light irradiation with various power intensities; (b) $I-T$ responses of the pn photodetector at 0 V with various power intensities; (c) photocurrent and responsivity as a function of the power intensities at 0 V; (d) detectivity as a function of the power intensities at 0 V; (e) I–T responses of the photodetector at various biases with 1000 μW/cm^2 light-254 nm illumination; (f) the response time of the photodetector under 1000 μW/cm^2 light-254 nm illumination at 0 V.

Fig. 6. (a) $I-V$ characteristics of the CuCrO$_2$/β-Ga$_2$O$_3$ pn photodetector under 254 nm light irradiation with various power intensities; (b) $I-T$ responses of the pn photodetector at 0 V with various power intensities; (c) photocurrent and responsivity as a function of the power intensities at 0 V; (d) detectivity as a function of the power intensities at 0 V; (e) I–T responses of the photodetector at various biases with 1000 μW/cm^2 light-254 nm illumination; (f) the response time of the photodetector under 1000 μW/cm^2 light-254 nm illumination at 0 V.

more detailed research, the photoresponse time under a 0 V bias is fitted to calculate the response time using a second-order exponential equation. The rise and decay times are about 0.26 s/0.14 s at 0 V, which are given in Fig. 5f.

The representative $I-V$ and $I-T$ characteristics of the CuCrO$_2$/β-Ga$_2$O$_3$ pn photodetector were researched and are presented in Fig. 6. The photodetector exhibits an I_{on}/I_{off} of 3.5 $\times$ 10^4 at a 1000 μW/cm^2 light intensity density. As shown in Fig. 6c and d, at

zero bias, the R and D of the photodetector achieve maximum values of 0.12 mA/W and 4.6 $\times$ 10^{11} Jones at 50 μW/cm^2 light, respectively. The rise and decay times are about 0.35 s/0.06 s for the CuCrO$_2$/β-Ga$_2$O$_3$ pn photodetector. The photocurrent of the photodetectors under 365 nm light irradiation are measured and listed in SFigure 6, which exhibit a limited photocurrent of a few fA. Thus, the rejection ratio (R$_{254}$/R$_{365}$) of the pn junction photodetector with 1000 μW/cm^2 illumination at 0 V can reach 2 $\times$ 10^4 (CuGaO$_2$/β-
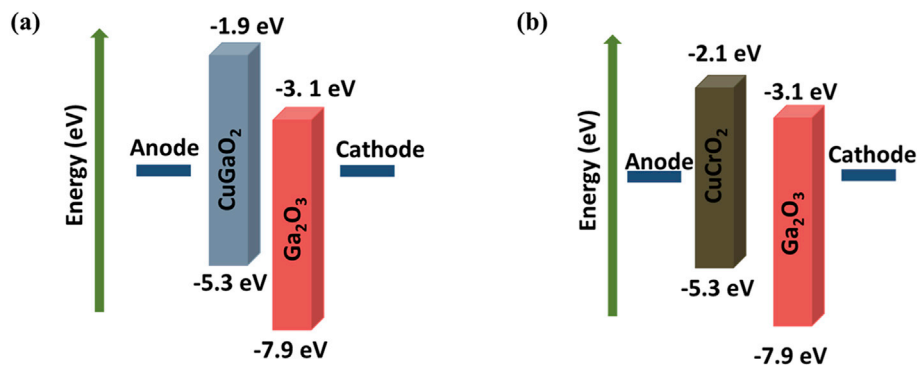
Fig. 7. Energy band diagrams of the (a) CuGaO$_2$/β-Ga$_2$O$_3$ pn junction and (b)CuCrO$_2$/β-Ga$_2$O$_3$ pn junction.

Table 1
The self-powered device parameters comparison of photodetectors based on Ga$_2$O$_3$ from previous works and this work.

Materials	I_{off} (A)	I_{on}/I_{off}	Response time (s)	Rejection ratio	Ref
Ga$_2$O$_3$/ZnO	$\approx 10^{-9}$	127	0.27	690(R$_{251}$/R$_{400}$)	[60]
Ga$_2$O$_3$/p-Si	$\approx 10^{-8}$	940	1.80	1×10^3 (R$_{254}$/R$_{400}$)	[61]
Ga$_2$O$_3$/NSTO	$\approx 10^{-6}$	20	0.07	/	[11]
Graphene/Ga$_2$O$_3$	$\approx 10^{-9}$	83	0.96	/	[62]
Ga$_2$O$_3$/SiC	$\approx 10^{-10}$	3.8	0.31	/	[63]
Ga$_2$O$_3$/GaN	$\approx 10^{-10}$	5	0.08	152 (R$_{254}$/R$_{400}$)	[64]
Sn:Ga$_2$O$_3$/GaN	$\approx 10^{-11}$	10^4	0.02	6×10^3 (R$_{254}$/R$_{365}$)	[12]
Ga$_2$O$_3$/Diamond	$\approx 10^{-9}$	37	/	135 (R$_{254}$/R$_{400}$)	[15]
Ga$_2$O$_3$/CuSCN	$\approx 10^{-12}$	4.1×10^4	0.04	1×10^4 (R$_{254}$/R$_{365}$)	[58]
Ga$_2$O$_3$/CuCrO$_2$	$\approx 10^{-14}$ (0 V)	3.5×10^4	0.06	2.8×10^4 (R$_{254}$/R$_{365}$)	This work
Ga$_2$O$_3$/CuGaO$_2$	$\approx 10^{-14}$ (0 V)	2.3×10^4	0.14	2.0×10^4 (R$_{254}$/R$_{365}$)	This work

Ga$_2$O$_3$) and 2.8×10^4 (CuCrO$_2$/β-Ga$_2$O$_3$), presenting a high spectral selectivity. SFigure 7 show the responsivity curves of the devices at a bias of -5 V. The maximum responsivity of the both two devices are located at 250 nm, which corresponds to the optical absorption edge of Ga$_2$O$_3$ film. The result indicates that the photogenerated carriers of the devices are mainly excited by solar-blind radiation with a higher energy than Ga$_2$O$_3$ bandgap. The photoresponses of the two devices are much larger under solar-blind radiation (<280 nm) than under UVB (280−320 nm) and UVA (320−400 nm).

To fully understand the intrinsic physical mechanism of the self-powered CuGaO$_2$/β-Ga$_2$O$_3$ and CuCrO$_2$/β-Ga$_2$O$_3$ photodetectors, the corresponding schematic diagrams of the charge carrier transport and pn junction energy band are depicted in Fig. 7. The band energy level positions of the β-Ga$_2$O$_3$ film and CuGaO$_2$ and CuCrO$_2$ were obtained according to literature reports [48,57−59]. Combined with the measured bandgap values, the CB/VB of β-Ga$_2$O$_3$, CuGaO$_2$ and CuCrO$_2$ is 3.1/7.9 eV, 1.9/5.3 eV and 2.1/5.3 eV, respectively. Consequently, once β-Ga$_2$O$_3$ is put in contact with CuGaO$_2$ or CuCrO$_2$, a classic type II heterojunction is built (Fig. 7a and b). Upon light illumination, considerable electron-hole pairs will be generated and then separate quickly under the driving force of the built-in field. These photo-induced charge carriers will form a large photocurrent even without an applied voltage, which can support the self-powered operation of the photodetector.

Comparisons between the devices in this work and some previous reports are listed in Table 1. As solar-blind photodetectors, the CuMO$_2$/β-Ga$_2$O$_3$ pn photodetectors show a low dark current, a high I_{on}/I_{off} and a superhigh rejection ratio at 0 Vcompared to some other photodetectors. In addition, the lifetime reliability and device stability of our achieved photodetectors were tested over a duration of one month with normal atmospheric storage. The photodetectors retain sensitivity to the solar-blind signal and an almost unchanged photocurrent (SFigure 8). Such excellent device reliability benefits from the material stability of the β-Ga$_2$O$_3$ and CuMO$_2$.

3. Conclusion

In this study, highly crystalline CuMO$_2$ (M = Ga^{3+}, Cr^{3+}) are synthesized successfully by a simple and low-cost hydrothermal method and spin-coated on a β-Ga$_2$O$_3$ epitaxial film to construct CuGaO$_2$/β-Ga$_2$O$_3$ and CuCrO$_2$/β-Ga$_2$O$_3$ pn photodetectors. The matched band alignment enables the well-designed photodetectors to work in energy saving mode. The CuGaO$_2$/β-Ga$_2$O$_3$ and CuCrO$_2$/β-Ga$_2$O$_3$ photodetector show remarkable properties, such as an ultralow off state current of 51 fA/61 fA, a superhigh off-to-on state current ratio of 2.3×10^4/3.5×10^4, a high detectivity value of 0.9×10^{11}/4.7×10^{11} Jones and a high rejection ratio of 2×10^4/2.8×10^4. Meanwhile, these pn photodetectors possess ultrastable reliability even after one month. These simple, low-cost, high-performance and stable pn heterojunction self-powered photodetectors have great potential applications in solar-blind light detection systems.

4. Experimental Section

Synthesis of CuMO$_2$: The hydrothermal synthesis process of CuGaO$_2$ and CuCrO$_2$ are modified from the previous reports. For CuGaO$_2$ micro-plates, in a typical synthesis, briefly, precursor solution is consisted of 2.8 mmol Ga(NO$_3$)$_3$·xH$_2$O, 2.8 mmol Cu(NO$_3$)$_2$·3H$_2$O, 24 mL deionized water, 16 mL ethylene glycol and 12 mL 0.5 m KOH. Then, the Teflon autoclave filled with precursor solution was maintained at 200 °C for 24 h. The obtained CuGaO$_2$ precipitate was washed with diluted NH$_3$·H$_2$O, HNO$_3$ solution and deionized water several. The obtained CuGaO$_2$ micro-plates need store in absolute isopropanol solution for further use. For CuCrO$_2$ nanocrystals, precursor solution is consisted of 15 mmol Cr(NO$_3$)$_3$·9H$_2$O and 15 mmol Cu(NO$_3$)$_2$·3H$_2$O, 5.0 g NaOH and 70 mL deionized water. The Teflon autoclave was maintained at 240 °C for 60 h. Then obtained CuCrO$_2$ precipitate was washed and

stored as mentioned above.

Synthesis of Ga₂O₃ Thin Films: The MOCVD growth unintentionally doped Ga₂O₃ thin films were obtained from the Beijing Gallium Family Technology Ltd. The thickness of the as-grown Ga₂O₃ film was approximately 450 nm.

Fabrication of CuGaO₂@β-Ga₂O₃ and CuCrO₂@β-Ga₂O₃ Photodetectors: To fabricate the devices, an 2-inch Ga₂O₃ film was cut into 10 × 10 mm pieces by a laser cutting machine. Then the CuGaO₂/CuCrO₂ isopropanol solution (10 mg/ml) was spin coated on the Ga₂O₃ film at 3000 rpm for 40 s. After releasing the tape at 150 °C for 1 min, square electrodes of 30 nm Ti and 70 nm Au were deposited on the surface of the Ga₂O₃ region by the RF magnetron sputtering method using a metal mask.

Material Characterization: The structure and morphology of the CuGaO₂/CuCrO₂ were characterized by field-emission SEM (S4800, Hitachi) and TEM (JEM-2100). The phase of CuGaO₂/CuCrO₂ and Ga₂O₃ was checked by an X-ray diffractometer (D8 Discover, Cu Kα radiation, λ = 0.15 418 nm). Absorption spectra were obtained by a UV-VIS spectrophotometer (U-3900). Chemical analysis was performed with an XPS system (K-Alpha). The morphology of the Ga₂O₃ films was characterized by AFM (XE100E).

Photoelectrical Measurements: The $I-V$ characteristics and time-dependent curves of all the photodetectors were measured using a Keithley 4200-SCS. For comparison, Ga₂O₃, CuGaO₂ and CuCrO₂ devices with metal-semiconductor-metal (MSM) structures were also prepared and measured. All characterizations and measurements were performed under room temperature and ambient conditions.

Author contribution

Daoyou Guo, Fengmin Wu, Pingfan Du and Weihua Tang: Conceptualization, Methodology, Chao Wu, Linlin Qiu, Shan Li and Zhengwei Chen: Investigation, Writing- Original draft preparation. Shunli Wang and Daoyou Guo: Supervision. Chao Wu, Xianghu Wang, Huaping Wu, Peigang Li and Aiping Liu: Writing-Reviewing and Editing. Daoyou Guo, Aiping Liu and Fengmin Wu: Project administration, Funding acquisition.

Declaration of competing interest

The authors declare no conflict of interest.

Acknowledgements

Appendix A. Supplementary data

Supplementary data to this article can be found online at https://doi.org/10.1016/j.mtphys.2020.100335.

References

[1] Y.C. Chen, Y.J. Lu, Q. Liu, C.N. Lin, J. Guo, J.H. Zang, Y.Z. Tian, C.X. Shan, J. Mater. Chem. C 7 (2019) 2557−2562.
[2] Y.C. Chen, Y.J. Lu, C.N. Lin, Y.Z. Tian, C.J. Gao, L. Dong, C.X. Shan, J. Mater. Chem. C 6 (2018) 5727−5732.
[3] C. Lin, Y. Lu, Y. Tian, C. Gao, M. Fan, X. Yang, L. Dong, C. Shan, Optic Express 27 (2019) 29962−29971.
[4] J. Yu, C.X. Shan, J.S. Liu, X.W. Zhang, B.H. Li, D.Z. Shen, Phys. Status Solidi-R 7 (2013) 425−428.
[5] W. Yang, S.S. Hullavarad, B. Nagaraj, I. Takeuchi, R.P. Sharma, T. Venkatesan, R.D. Vispute, H. Shen, Appl. Phys. Lett. 82 (2003) 3424−3426.
[6] Z.G. Shao, D.J. Chen, H. Lu, R. Zhang, D.P. Cao, W.J. Luo, Y.D. Zheng, L. Li, Z.H. Li, IEEE Electron. Device Lett. 35 (2014) 372−374.
[7] E. Monroy, F. Omnes, F. Calle, Semicond. Sci. Technol. 18 (2003) R33.
[8] D. Zhang, W. Lin, S. Liu, Y. Zhu, R. Lin, W. Zheng, F. Huang, ACS Appl. Mater. Interfaces 11 (51) (2019) 48071−48078.
[9] C. Wu, C.R. He, D.Y. Guo, F.B. Zhang, P.G. Li, S.L. Wang, A.P. Liu, F.M. Wu, W.H. Tang, Mater. Today Phys. 12 (2020) 100193.
[10] C.R. He, D.Y. Guo, K. Chen, S.L. Wang, J.Q. Shen, N. Zhao, A.P. Liu, Y. Zheng, P.G. Li, Z. Wu, C.R. Li, F.M. Wu, W.H. Tang, ACS Appl. Nano Mater. 2 (2019) 4095−4103.
[11] D.Y. Guo, H. Liu, P.G. Li, Z. Wu, S.L. Wang, C. Cui, C.R. Li, W.H. Tang, ACS Appl. Mater. Interfaces 9 (2017) 1619−1628.
[12] D.Y. Guo, Y.L. Su, H.Z. Shi, P.G. Li, N. Zhao, J. Ye, S.L. Wang, A.P. Liu, Z. Chen, C. Li, W.H. Tang, ACS Nano 12 (2018) 12827−12835.
[13] D.Y. Guo, Q.X. Guo, Z. Chen, Z. Wu, P.G. Li, W.H. Tang, Mater. Today Phys. 11 (2019) 100157.
[14] P.G. Li, H.Z. Shi, K. Chen, D.Y. Guo, W. Cui, Y.S. Zhi, S.L. Wang, Z.P. Wu, Z.W. Chen, W.H. Tang, J. Mater. Chem. C 5 (2017) 10562−10570.
[15] Y. Chen, Y. Lu, M. Liao, Y. Tian, Q. Liu, C. Gao, X. Yang, C. Shan, Adv. Funct. Mater. 29 (2019) 1906040.
[16] M. Yu, C. Lv, J. Yu, Y. Shen, L. Yuan, J. Hu, S. Zhang, H. Cheng, Y. Zhang, R. Jia, Mater. Today Commun. 25 (2020) 101532.
[17] H.P. Zhang, L. Yuan, X.Y. Tang, J.C. Hu, J.W. Sun, Y.M. Zhang, Y.M. Zhang, R.X. Jia, IEEE Trans. Power Electron. 35 (5) (2020) 5157.
[18] S. Luan, L. Dong, X. Ma, R. Jia, J. Alloys Compd. 812 (2019) 152026.
[19] C. Wu, D.Y. Guo, L.Y. Zhang, P.G. Li, F.B. Zhang, C.K. Tan, S.L. Wang, A.P. Liu, F.M. Wu, W.H. Tang, Appl. Phys. Lett. 116 (2020): 072102.
[20] F. Alema, B. Hertog, A. Osinsky, P. Mukhopadhyay, M. Toporkov, W.V. Schoenfeld, J. Cryst. Growth 475 (2017) 77−82.
[21] S. Rafique, L. Han, A.T. Neal, S. Mou, M.J. Tadjer, R.H. French, H. Zhao, Appl. Phys. Lett. 109 (2016) 132013.
[22] S. Luan, L. Dong, X. Ma, R. Jia, J. Alloys Compd. 812 (2020) 152026.
[23] D.J. Comstock, J.W. Elam, Chem. Mater. 24 (2012) 4011−4018.
[24] R. Lin, Q. Guo, Q. Zhu, Y. Zhu, W. Zheng, F. Huang, Adv. Mater. 31 (2019): e1905079.
[25] N. Ma, K. Zhang, Y. Yang, Adv. Mater. 29 (2017) 1703694.
[26] B.S. Ouyang, K.W. Zhang, Y. Yang, Adv. Mater. Technol. 2 (2017) 1700208.
[27] J. Qi, N. Ma, X.C. Ma, R. Adelung, Y. Yang, ACS Appl. Mater. Interfaces 10 (16) (2018) 13712−13719.
[28] J. Qi, N. Ma, Y. Yang, Adv. Mater. Interfaces 5 (2018) 1701189.
[29] T.T. Gao, Y. Ji, Y. Yang, Adv. Electron. Mater (2019) 1900776.
[30] B.S. Ouyang, K.W. Zhang, Y. Yang, iScience 2 (2018) 86.
[31] B.S. Ouyang, C. Chang, L.D. Zhao, Z.L. Wang, Y. Yang, Nanomater. Energy 66 (2019) 104111.
[32] Y.T. Jiang, Y. Wang, H.T. Wu, Y.H. Wang, R.Y. Zhang, H.K. Olin, Y. Yang, Nano-Micro Lett. 11 (2019) 99.
[33] B.S. Ouyang, H.Q. Zhao, Z.L. Wang, Y. Yang, Nanomater. Energy 68 (2020) 104312.
[34] J.G. Yu, M. Yu, Z. Wang, L. Yuan, Y.C. Huang, L. Zhang, Y.M. Zhang, R.X. Jia, IEEE Electron. Device Lett. 67 (2020) 3199−3204.
[35] T. Yang, X. Li, L. Wang, Y. Liu, K. Chen, X. Yang, L. Liao, L. Dong, C.X. Shan, J. Mater. Sci. 54 (2019) 14742−14751.
[36] Z. Wu, L. Jiao, X. Wang, D. Guo, W. Li, L. Li, F. Huang, W. Tang, J. Mater. Chem. C 5 (2017) 8688−8693.
[37] Y.W. Wang, C. Wu, D.Y. Guo, P.G. Li, S.L. Wang, A.P. Liu, C. Li, F.M. Wu, W.H. Tang, ACS Appl. Electron. Mater. 2 (7) (2020) 2032−2038.
[38] P.A. Shaikh, V.P. Thakare, D.J. Late, S. Ogale, Nanoscale 6 (2014) 3550−3556.
[39] M. Kumar, H. Zhao, C. Persson, Semicond. Sci. Technol. 28 (2013): 065003.
[40] M. Yu, T.I. Draskovic, Y. Wu, Phys. Chem. Chem. Phys. 16 (2014) 5026−5033.
[41] Y.J. Lin, J. Luo, H.C. Hung, Appl. Phys. Lett. 102 (2013) 193511.
[42] A. Forticaux, S. Hacialioglu, J.P. DeGrave, R. Dziedzic, S. Jin, ACS Nano 7 (2013) 8224−8232.
[43] S. Dursun, I.C. Kaya, V. Kalem, H. Akyildiz, Dalton Trans. 47 (2018) 14662−14678.
[44] T. Omata, H. Nagatani, I. Suzuki, M. Kita, H. Yanagi, N. Ohashi, J. Am. Chem. Soc. 136 (2014) 3378−3381.
[45] A. Renaud, L. Cario, P. Deniard, E. Gautron, X. Rocquefelte, Y. Pellegrin, E. Blart, F. Odobel, S. Jobic, J. Phys. Chem. C 118 (2013) 54−59.
[46] L. Shi, F. Wang, Y. Wang, D. Wang, B. Zhao, L. Zhang, D. Zhao, D. Shen, Sci. Rep. 6 (2018) 21135.
[47] J. Wang, V. Ibarra, D. Barrera, L. Xu, Y.J. Lee, J.W. Hsu, J. Phys. Chem. Lett. 6 (2015) 1071−1075.
[48] D. Xiong, H. Chang, Q. Zhang, S. Tian, B. Liu, X. Zhao, Appl. Surf. Sci. 347 (2015) 747−754.
[49] D. Xiong, Z. Xu, X. Zeng, W. Zhang, W. Chen, X. Xu, M. Wang, Y.B. Cheng, J. Mater. Chem. 22 (2012) 24760−24768.
[50] Z. Xu, D. Xiong, H. Wang, W. Zhang, X. Zeng, L. Ming, W. Chen, X. Xu, J. Cui, M. Wang, S. Powar, U. Bach, Y.B. Cheng, J. Mater. Chem. 2 (2014) 2968−2976.
[51] H. Zhang, H. Wang, H. Zhu, C.-C. Chueh, W. Chen, S. Yang, A.K.Y. Jen, Adv. Energy Mater. 8 (2018) 1702762.
[52] Y. Li, Y. Song, Y. Jiang, M. Hu, Z. Pan, X. Xu, H. Chen, Y. Li, L. Hu, X. Fang, Adv. Funct. Mater. 27 (2017) 1701066.

[53] C.Y. Tsay, C.L. Chen, J. Cryst. Growth 468 (2017) 662−665.

[54] X. Wang, H. Wu, G. Wang, X. Ma, Y. Xu, H. Zhang, L. Jin, L. Shi, Y. Zou, J. Yin, D. Zhao, Phys. Status Solidi 257 (2020) 1900684.

[55] Y. Chen, Z. Yang, S. Wang, X. Zheng, Y. Wu, N. Yuan, W.H. Zhang, S.F. Liu, Adv. Mater. 30 (2018): e1805660.

[56] M. Yu, T.I. Draskovic, Y. Wu, Inorg. Chem. 53 (2014) 5845−5851.

[57] H. Zhang, H. Wang, W. Chen, A.K. Jen, Adv. Mater. 29 (2017) 1604984.

[58] S. Li, D. Guo, P. Li, X. Wang, Y. Wang, Z. Yan, Z. Liu, Y. Zhi, Y. Huang, Z. Wu, W. Tang, ACS Appl. Mater. Interfaces 11 (2019) 35105−35114.

[59] J. Ma, M. Zheng, C. Chen, Z. Zhu, X. Zheng, Z. Chen, Y. Guo, C. Liu, Y. Yan, G. Fang, Adv. Funct. Mater. 28 (2018) 1804128.

[60] Z. Wu, L. Jiao, X. Wang, D. Guo, W. Li, L. Li, F. Huang, W. Tang, J. Mater. Chem. C 5 (34) (2017) 8688−8693.

[61] X.C. Guo, N.H. Hao, D.Y. Guo, Z.P. Wu, Y.H. An, X.L. Chu, L.H. Li, P.G. Li, M. Lei, W.H. Tang, J. Alloys Compd. 660 (2016) 136−140.

[62] M. Ai, D. Guo, Y. Qu, W. Cui, W. Tang, J. Alloys Compd. 692 (2017) 634−638.

[63] J.G. Yu, L. Dong, B. Peng, L. Yuan, R. Jia, J. Alloys Compd. 821 (2019) 153532.

[64] T. He, X. Zhang, X. Ding, C. Sun, Y. Zhao, Q. Yu, J. Ning, R. Wang, G. Yu, S. Lu, Adv. Opt. Mater. 7 (2019) 1801563.